

High performance MnO₂ nanoflower supercapacitor electrode by electrochemical recycling of spent batteries



Gomaa A.M. Ali^{a,b}, Mashitah M. Yusoff^a, Essam R. Shaaban^c, Kwok Feng Chong^{a,*}

^a Faculty of Industrial Sciences and Technology, Universiti Malaysia Pahang, Gambang, 26300 Kuantan, Malaysia

^b Chemistry Department, Faculty of Science, Al-Azhar University, Assiut 71524, Egypt

^c Physics Department, Faculty of Science, Al-Azhar University, Assiut 71524, Egypt

ARTICLE INFO

Keywords:

Spent batteries
Supercapacitance
Electrochemical conversion
MnO₂ nanoflower

ABSTRACT

MnO₂ nanoflower is prepared by electrochemical conversion of Mn₃O₄ obtained by heat treatment of spent zinc–carbon batteries cathode powder. The heat treated and converted powders were characterized by TGA, XRD, FTIR, FESEM and TEM techniques. XRD analyses show formation of Mn₃O₄ and MnO₂ phases for the heat treated and converted powders, respectively. FESEM images indicate the formation of porous nanoflower structure of MnO₂, while, condensed aggregated particles are obtained for Mn₃O₄. The energy band gap of MnO₂ is obtained from UV–Vis spectra to be 2.4 eV. The electrochemical properties are investigated using cyclic voltammetry, galvanostatic charge–discharge and electrochemical impedance techniques using three-electrode system. The specific capacitance of MnO₂ nanoflower (309 F g^{−1} at 0.1 A g^{−1}) is around six times higher than those obtained from the heat treated one (54 F g^{−1} at 0.1 A g^{−1}). Moreover, it has high capacitance retention up to 93% over 1650 cycles. Impedance spectra of MnO₂ nanoflower show very small resistances and high electrochemical active surface area (340 m² g^{−1}). The present work demonstrates a novel electrochemical approach to recycle spent zinc–carbon batteries into high value supercapacitor electrode.

1. Introduction

The literature survey of supercapacitors shows that a variety of metal oxide has been employed. To improve the current supercapacitor technology, it is essential to use high–capacitance materials with new morphologies. Transition metal oxides are widely used as supercapacitor materials because of their pseudocapacitance, good capacitance retention and high rate performance [1–9]. Among all the metal oxides that can be used for supercapacitor, manganese oxide (MnO₂) has attracted great attention due to its high capacitance, environmental benignity and natural abundance [4,10–12]. The cost is a crucial role in any preparation process, so choosing the best precursor which has lower cost is a very important factor.

Zinc–carbon (Zn–C) dry cell batteries are widely used in different household applications. These batteries are not rechargeable and are discarded when fully discharged. Spent dry cell batteries contain significant quantities of manganese that can be technically extracted and reused as well as it could be considered as costless. Recycling of these wastes would offer economic benefits through the recovery of the valuable materials, as well as the preservation of raw materials in the interest of the sustainable development. Pyrometallurgy and

hydrometallurgy methods are well-known methods in metals recovery [13]. In pyrometallurgy, the metal recovered by treatment of the spent batteries at high temperature, while solvents must be used in the hydrometallurgy process.

MnO₂ has an excellent capacitive performance in the aqueous electrolytes so it is widely used as electrode material for supercapacitors applications [2,4,14–16]. Many methods have been reported to prepare MnO₂, such as facile hydrothermal [16,17], sol–gel [18], electrodeposition [2,5,14,19,20] as well as the electrochemical oxidation techniques [21,22]. Although, the recovery of manganese from the spent batteries has been widely studied [23–25], no papers report on the electrochemical conversion of Mn₃O₄ in spent batteries into MnO₂.

In this paper, MnO₂ is obtained from the heat treated cathode powder of spent Zn–C batteries using electrochemical conversion techniques. The heat treated and electrochemical converted powders were characterized using TGA, XRD, FTIR, FESEM and TEM techniques. The electrochemical properties were investigated using cyclic voltammetry (CV), galvanostatic charge–discharge (GCD) and electrochemical impedance spectroscopy (EIS).

* Corresponding author.

E-mail address: ckfeng@ump.edu.my (K.F. Chong).

<http://dx.doi.org/10.1016/j.ceramint.2017.03.195>

Received 1 February 2017; Received in revised form 12 March 2017; Accepted 30 March 2017

Available online 31 March 2017

0272-8842/ © 2017 Elsevier Ltd and Techna Group S.r.l. All rights reserved.

2. Experimental procedures and techniques

2.1. Samples preparation

2.1.1. Batteries dismantling and pre-treatment

Spent cylindrical 1.5 V D-type Zn–C batteries (EVEREADY®) were collected from a collection point where people throw spent batteries and used for this study. Dismantled products such as plastic films, ferrous scraps, paper pieces and the anodic mixture were separated from the cathode black paste and it was used for further processing. The mass of the paste was about 76% of the total battery weight. The black paste was dried for 24 h at 130 °C. The weight of the dried paste showed a weight loss of 19.56%. The paste was subsequently ground and sieved using a 200 µm standard sieve. The retention mass ratios of –200 µm and +200 µm were 91.58% and 8.42%, respectively. The dry powder (50 g) was washed with distilled water at 60 °C (solid to liquid ratio 1:10) for 1 h. After contact time of 1 h, the solution was filtered at pH 6.8. The purpose of this washing is to remove the residue NH₄Cl in the battery electrolyte. Washed powder was dried for 24 h at 105 °C, recovered and weighted (46.3 g) with the weight loss of 7.4%.

2.1.2. Electrochemical cycling test

The dried battery powder was calcined at 900 °C to obtain the single phase of Mn₃O₄ (the dried sample was coded as CP900). The prepared Mn₃O₄ was used to make a film on Ni foam without any binder, which acted as working electrode in the electrochemical conversion cell. Mn₃O₄ was electrochemically converted to MnO₂ by CV in 1 M Na₂SO₄ electrolyte within a potential window of –0.1 to 0.9 V for 1000 cycles at 50 mV s^{–1}. The obtained material was coded as NF–MnO₂.

2.2. Samples characterization

Thermal behavior of the material was investigated using a Perkin Elmer Inc Pyris 1 TGA analyzer thermal gravimetric analysis, USA. Phase identification purity and particle size of the materials were measured at room temperature using a Rigaku Miniflex II X-Ray Diffractometer, Japan equipped with an automatic divergent slit. Diffraction patterns were obtained using Cu–K_α radiation (λ=0.15418 nm) and a graphite monochromator. The functional groups were examined using a Perkin Elmer Spectrum 100 spectrophotometer, USA over the range of 400–4000 cm^{–1}. Morphology of the materials was analysed using a JEOL JSM–7800 F, FESEM, USA field emission scanning electron microscope operating at 30.0 kV and a JEOL JEM2100F, TEM, USA transition electron microscopy at an accelerating voltage of 300 kV. The surface area of NF–MnO₂ was measured by NOVA 3200 surface area analyzer.

2.3. Optical measurements

The UV–Vis absorption spectra were obtained in the wavelength range from 200 to 900 nm at room temperature using a Thermo Scientific UV–Vis spectrophotometer, USA with a quartz cell. Measurements were made by suspending about 1 mg sample in 10 mL of absolute ethanol.

2.4. Supercapacitance measurements

The electrochemical properties were measured by three-electrode system, which consisted of the active material as working electrode, Ag/AgCl (CH Instrument) as reference electrode and Pt wire (CH Instrument) as counter electrode. The data were collected using an electrochemical workstation (Autolab/PGSTAT M101) equipped with frequency response analyzer. CV tests were performed in the potential range between 0 and 1 V with scan rates from 5 to 100 mV s^{–1}. GCD tests were performed at different current densities. Impedance data were collected from 50 kHz to 0.01 Hz, at open circuit potential (OCP) with AC amplitude of 10 mV. Mott–Schottky data were collected by testing the impedance under different applied potentials to determine the flat band potential.

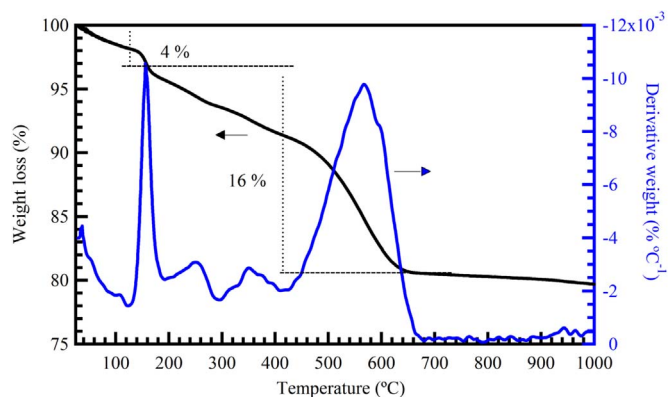


Fig. 1. TGA and DTA curves for dry cathode powder.

3. Results and discussion

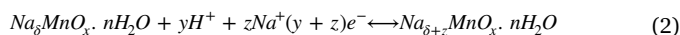
3.1. Structural and morphological analyses

3.1.1. Thermogravimetric analysis

Fig. 1 shows the thermogravimetric analysis (TGA) and differential thermal analysis (DTA) for the dry cathode powder. TGA shows that the presence of two weight loss stages, the first is about 4%, which refers to the surface adsorbed water elimination. The second stage is about 16% and it refers to the combustion of carbon [26] and conversion of all Mn phases into Mn₃O₄. These two stages are accompanied with two DTA peaks at 160 and 560 °C. Thus, the heat treatment temperature was chosen to be at 900 °C to eliminate most of the carbon content and to obtain a single phase of Mn.

3.1.2. Conversion of Mn₃O₄ into MnO₂

The electrochemical cycling conversion of Mn₃O₄ into MnO₂ includes two processes as follows [3,21,22]:



Reaction (1) represents the complex and irreversible process transformation of Mn₃O₄ to layered MnO₂. While, the reaction (2) is the reversible cycling of the latter material.

Fig. 2 shows the electrochemical cycling (conversion) from Mn₃O₄ (in CP900) into NF–MnO₂ in the voltage window from –0.1 to 0.9 V at 50 mV s^{–1} for 1000 cycles. The CV conversion was performed using three-electrode system cell which consists of working electrode (Mn₃O₄ on Ni foam), Pt counter electrode and Ag/AgCl reference electrode immersed in 1 M Na₂SO₄ solution. The current is increased by more than 100 times during the cycling process, which is clearly observed in

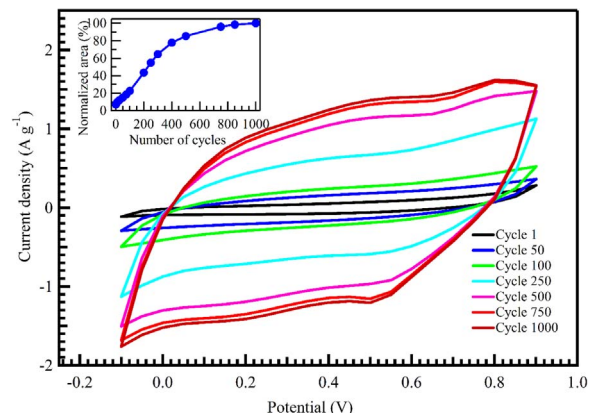
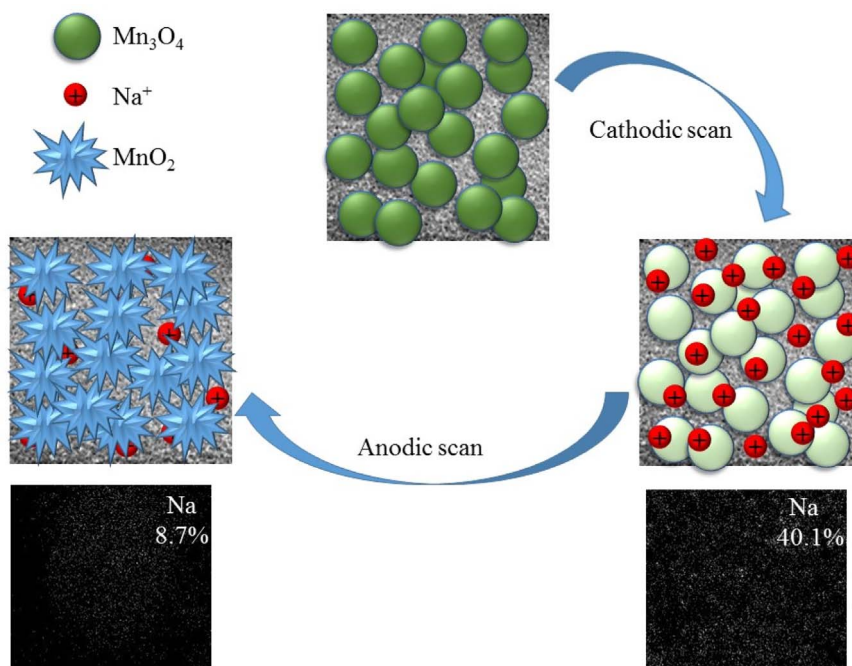


Fig. 2. CV electrochemical conversion of CP900 at 50 mV s^{–1} in 1 M Na₂SO₄.



Scheme 1. Graphical representation of the electrochemical preparation of MnO_2 nanoflower from Mn_3O_4 .

the CV over the entire potential range, particularly after the 500th cycle. As shown in the inset of Fig. 2, the normalized area under the CV curve is increased with increasing cycle number until it reaches a plateau after 750 cycles, indicating the complete conversion of Mn_3O_4 into NF- MnO_2 . This process is known as potential-dynamic activated procedure [15,21,22]. The electrochemical conversion process in Na_2SO_4 results in the formation of hydrated compounds with an extremely porous surface layer, which is useful for the energy storage application. Djurfors et al. [27] found that the oxidation of Mn occurs through the following sequence of oxides: Mn to MnO , to Mn_3O_4 , to Mn_2O_3 and finally to MnO_2 with complete oxidizing voltage of 0.9 V. Contrary to the common electro-winning method which only applies the positive potential, the current approach utilizes the anodic and cathodic scans in order to intercalate the Na^+ ions and oxidize the Mn constituents during CV process. Scheme 1 shows a graphical representation of the electrochemical preparation of NF- MnO_2 from Mn_3O_4 . During the cathodic scan, Na^+ ions are accumulated on the surface of Mn_3O_4 particles and simultaneously intercalated into the structure. During the anodic scan, Na^+ ions are repelled from the structure leaving a porous structure and the Mn_3O_4 is oxidized into MnO_2 . Continuous anodic/cathodic scans during CV cause the exfoliation of particles into the nanoflower morphology. This is confirmed by the EDX mapping where high percentage of Na could be found after cathodic scan and the Na content is reduced after anodic scan. Similar findings had been reported elsewhere [28].

3.1.3. X-Ray diffraction

CP900 shows peaks related to Mn_3O_4 phase (ICDD 00–086–2337) in XRD spectrum as shown in Fig. 3. This result indicates that pure single phase of orthorhombic crystalline Mn_3O_4 is successfully obtained by heat treatment of the cathode powder. It is clear that, Mn_3O_4 is converted into ramsdellite MnO_2 phase (ICDD 96–151–4228) after electrochemical conversion. Moreover, the diffraction peaks of Ni substrate are shown as well. The apparent crystallite size for Mn_3O_4 and MnO_2 was calculated according Scherrer formula [29] and found to be 71 and 58 nm, respectively. The larger size of Mn_3O_4 is due to the presence of particles agglomeration at high treatment temperature (900 °C).

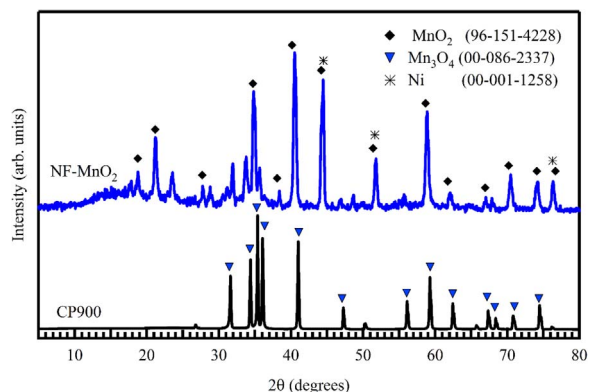


Fig. 3. XRD patterns of CP900 and NF- MnO_2 .

3.1.4. FTIR spectra

Fig. 4 shows FTIR spectra for CP900 and NF- MnO_2 . The two narrow and strong absorption bands at 620 and 510 cm^{-1} are assigned to the pairing mode between Mn–O stretching modes of tetrahedral and octahedral sites in Mn_3O_4 . Mn_3O_4 phase shows more intense bands. The small band at 1107 cm^{-1} is assigned to Mn–OH bending vibrations combined with Mn atoms [5,19]. It is obvious that the absorption bands at 3440 and 1635 cm^{-1} belong to the absorbed water molecules, indicating the hydrous nature of these materials. These bands are ascribed to the stretching of O–H mode of H-bonding and the bending of O–H mode of water molecules, respectively. The presence of Mn–OH and Mn–O bonds, which indicates the formation of hydrous MnO_2 may play important role in pseudocapacitive behavior.

3.1.5. FESEM and TEM

Fig. 5 shows FESEM images for CP900 and NF- MnO_2 . One can observe, fine and agglomerated aggregates in the heat treated cathode powder of CP900 (Fig. 5(a)), while the NF- MnO_2 shows nanoflower shape of MnO_2 nanoparticles with highly porous structure (Fig. 5(b)). Similar morphology is obtained for electrodeposited MnO_2 in other works [2,14]. This porous nanoflower morphology is highly preferable for electrochemical application, as the electrolyte ions could penetrate

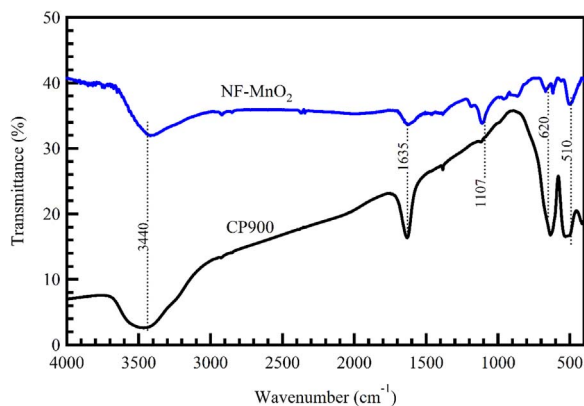


Fig. 4. FTIR spectra of CP900 and NF-MnO₂.

the pores and the electroactive centres could be generated. In addition, fine sheets and rod shapes of NF-MnO₂ is observed using TEM investigation as shown in Fig. 6 [17].

3.1.6. N₂ adsorption–desorption measurement

Fig. 7 shows the N₂ adsorption–desorption isotherm of NF-MnO₂ and its pores size distribution as inset. NF-MnO₂ shows a specific surface area of 42.6 m² g⁻¹ and pore size ranges from 1.5 to 12 nm (two narrow peaks around < 2 and 4 nm). These mesopores play an important role in enhancing ions adsorption during the electrochemical measurements by facilitating ions diffusion in the NF-MnO₂ structure.

3.2. Optical measurements

In nanomaterials, the optical band gap strongly depends on the particles size, where the smaller particles size shows wider band gap [30]. Fig. 8(a) shows the optical absorption spectra of the NF-MnO₂, where it exhibits a broad absorption band around 400 nm which is characteristic of the electronic transition between the valence and conduction bands consists primarily of an excitation from an O2p to Mn 3d state. Fig. 8(b) shows the relation between $(\alpha h\nu)^2$ vs. $h\nu$. The absorption coefficient (α) was calculated as reported elsewhere [31]. Extrapolation of the linear portion to zero absorption coefficient gives the value of the optical energy gap. It was found to be 2.4 eV, suggesting the direct transitions which are in good agreement with the MnO₂ band structure.

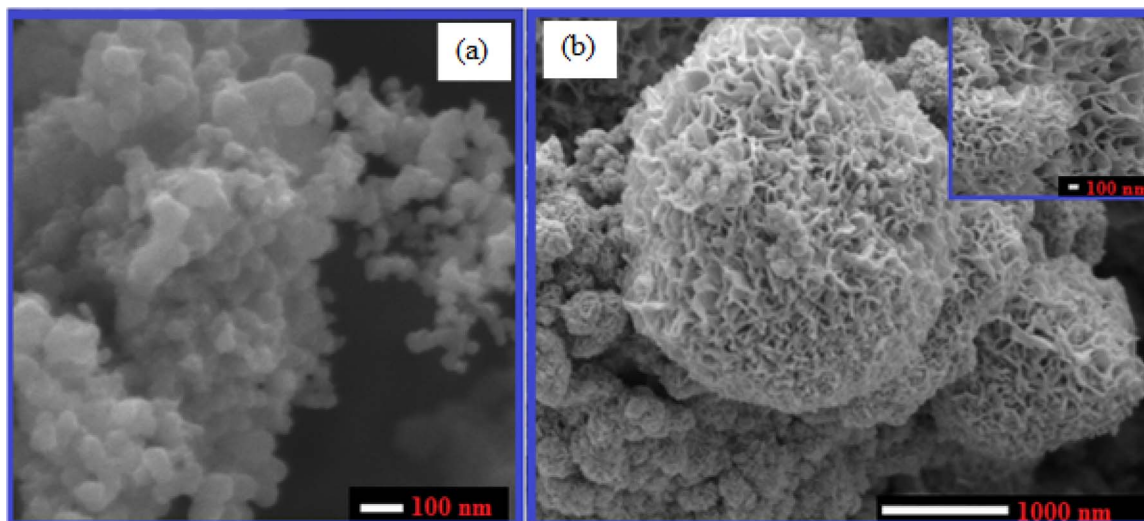


Fig. 5. FESEM images of (a) CP900 and (b) NF-MnO₂.

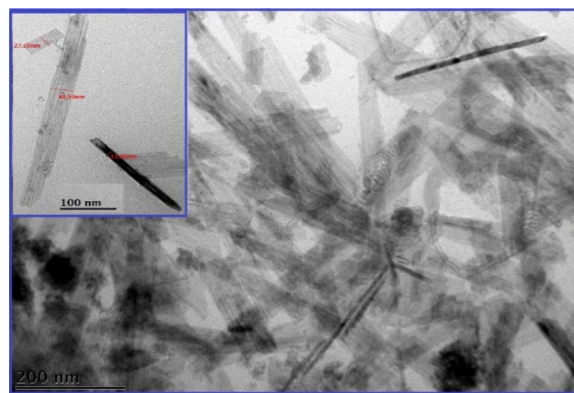


Fig. 6. TEM images of NF-MnO₂.

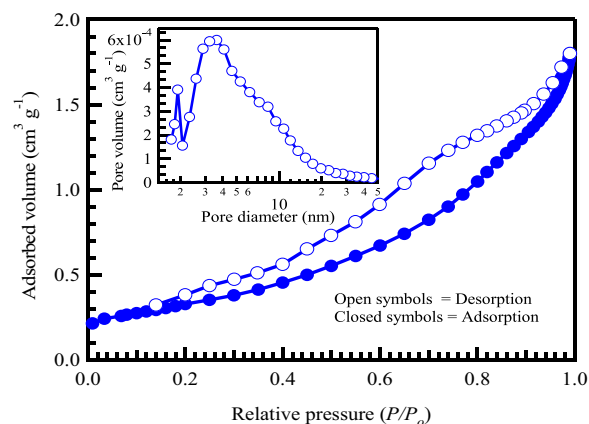


Fig. 7. N₂ adsorption–desorption isotherm; the inset shows the pores size distribution of NF-MnO₂.

3.3. Electrochemical properties

3.3.1. Cyclic voltammetry (CV) measurements

Fig. 9(a) shows CV curves at different scan rates for NF-MnO₂, which exhibit rectangular-shape voltammograms even at high scan rates. The area under the curve is increased with the increasing scan rate. Fig. 9(b) compares the CV curves at 25 mV s⁻¹ for NF-MnO₂ and CP900. One can observe that, the voltammogram of NF-MnO₂ is more rectangular and symmetrical around zero, indicates the enhanced capacitive properties and suggesting that the electrodes have high power characteristics which is an ideal supercapacitor behavior [21,22,32].

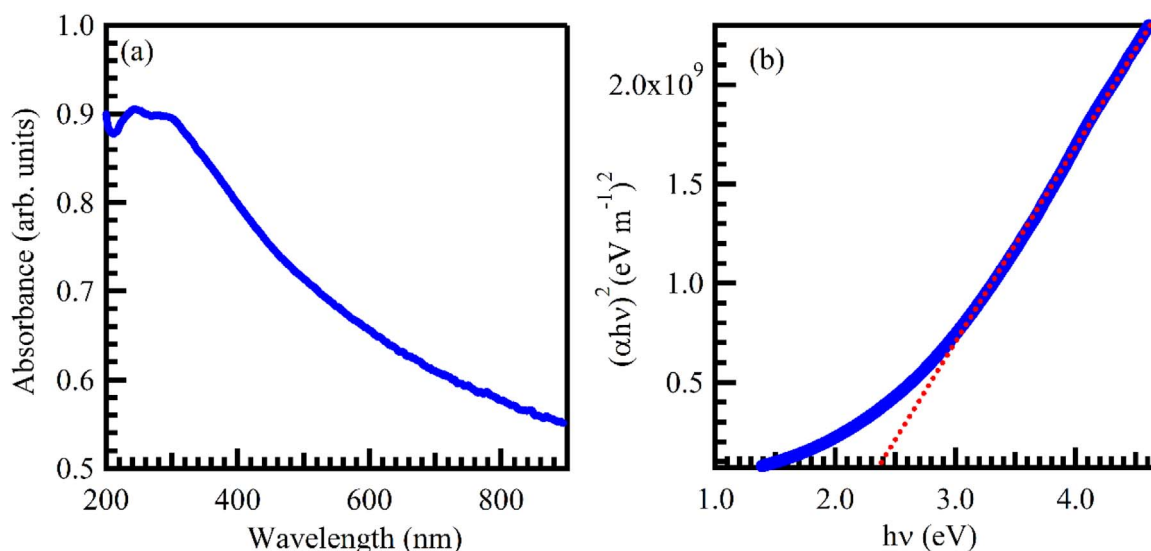


Fig. 8. Optical absorption spectra (a) and the direct transition $((\alpha h\nu)^2$ versus $h\nu$) curve (b) for NF-MnO₂.

3.3.2. Galvanostatic charge–discharge (GCD) measurements

Fig. 10(a) shows the charge–discharge curves at different current densities for NF-MnO₂ where it shows linear curves of charging and discharging at all current densities. The linear variation of potential during charging and discharging processes is another criterion for the capacitance behavior of the material in addition to exhibiting rectangular voltammograms. Very small (neglected) iR drop is observed in the discharge curves (1% at 0.25 A g⁻¹). The inset of Fig. 10(a) shows the charge–discharge curve at 0.25 A g⁻¹ of CP900 as compared to those for NF-MnO₂. The curves for NF-MnO₂ show wider time indicating higher charge accumulation. Fig. 10(b) shows the specific capacitance (C_s) as a function of current density calculated from the slope of charge–discharge curves according to Eq. (3) [21].

$$C_s = \frac{I}{m \cdot (dV/dt)} \quad (3)$$

where, I is the discharge current, dV/dt is the slope of discharge curve and m is the mass of active materials on the working electrode.

The C_s for NF-MnO₂ is found to be around 6 times higher (309 F g⁻¹ at 0.1 A g⁻¹) than that of CP900 (54 F g⁻¹ at 0.1 A g⁻¹) and it decreases with increasing current density. Table 1 compares the specific capacitance value of NF-MnO₂ with those reported for MnO₂ prepared from other sources and precursors. Aqueous electrolytes tend to produce faster charge–discharge rate due to the relatively high

conductivity and low viscosity of concentrated solutions. The faradaic-pseudocapacitance of MnO₂ could be attributed to two mechanisms. The first one is based on the intercalation and deintercalation of cations, during reduction and oxidation, respectively. The second is based on the adsorption of cations in the electrolyte ions on the MnO₂ surface, as shown in the following equations [5,16,19,32].



3.3.3. Stability study

NF-MnO₂ displays a good long-term cycle stability as shown in Fig. 11. At a higher current density (6 A g⁻¹), only about 7% decrease of the specific capacitance is observed after 1650 charge–discharge cycles, indicating the repetitive charge–discharges does not induce noticeable degradation of the microstructure. In addition, NF-MnO₂ shows a high ratio of Coulombic efficiency of 93%. The inset of Fig. 11 shows the 1st and the 1650th cycle of NF-MnO₂ in GCD cycling test and there is no significant difference between the first and the last cycle to indicate the high electrode stability.

3.3.4. Electrochemical impedance spectroscopy (EIS)

To investigate the electrochemical characteristics of the electrode–

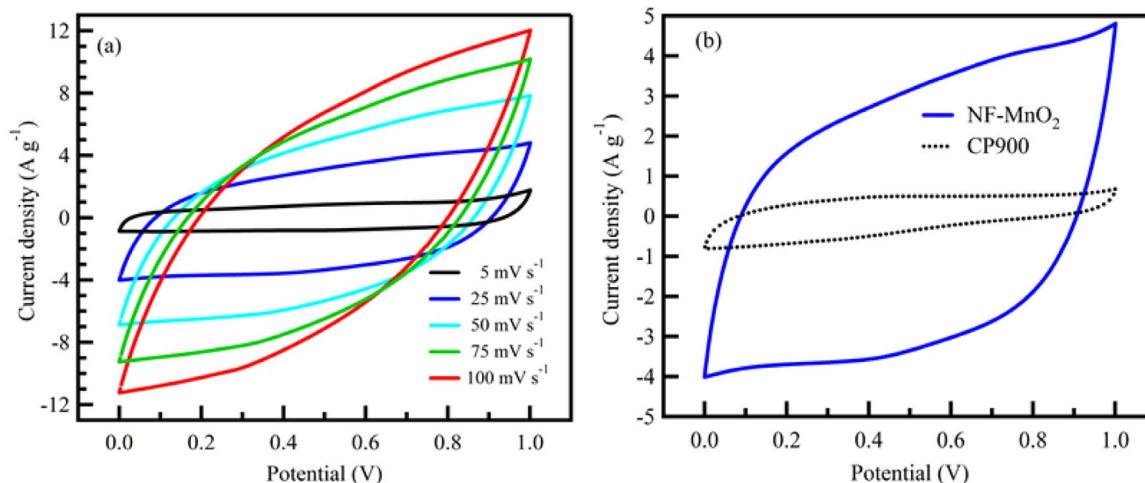


Fig. 9. CV curves for (a) NF-MnO₂ at different scan rates and (b) NF-MnO₂ and CP900 at 25 mV s⁻¹.

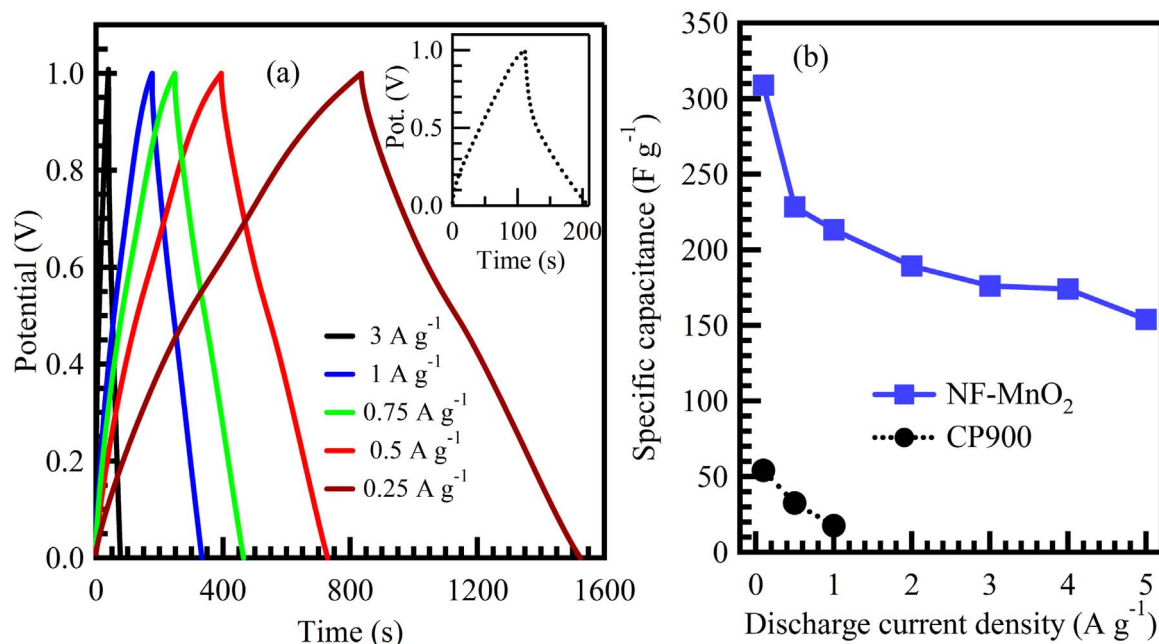


Fig. 10. (a) GCD curves for NF-MnO₂ at different current densities and (b) the specific capacitance as a function of current density NF-MnO₂ and CP900: The inset shows the charge-discharge curve of CP900 at 0.25 A g⁻¹.

Table 1

Comparison of reported specific capacitance with MnO₂ obtained from different precursors by different methods.

Precursor	Preparation Method	Specific capacitance (F g ⁻¹)	Reference
MnSO ₄ and K ₂ S ₂ O ₈	Hydrothermal	46 @ 5 mV s ⁻¹	[33]
MnSO ₄ and KMnO ₄	Hydrothermal	168 @ 1 mV s ⁻¹	[15]
KMnO ₄	Sol-gel route	150 @ 5 mV s ⁻¹	[34]
Mn(CH ₃ COO) ₂	Sol-gel template	165 @ 10 mV s ⁻¹	[18]
MnSO ₄ and KMnO ₄	Microemulsion	297 @ 1.075 A g ⁻¹	[35]
KMnO ₄	Galvanostatic electrodeposition	196 @ 1 A g ⁻¹	[14]
	Potentiostatic electrodeposition	128 @ 1 A g ⁻¹	
MnSO ₄	Potentiodynamic electrodeposition	237 @ 2 mA	[19]
	Potentiostatic electrodeposition	196 @ 2 mA	
	Galvanostatic electrodeposition	184 @ 2 mA	
Mn ₃ O ₄	Potential cycling	314 @ 5 mV s ⁻¹	[36]
	Cyclic voltammetry	133.1 @ 50 mV s ⁻¹	[3]
Manganese halide complex	Electrodeposition	108 @ 5 mV s ⁻¹	[37]
KMnO ₄ and MnCl ₂	Low temperature solid state reaction	258.7 @ 0.1 A g ⁻¹	[38]
Batteries	Leaching and electrowinning	294 @ 10 mV s ⁻¹	[2]
		208.5 @ 0.1 A g ⁻¹	
	Cyclic voltammetry conversion	309 @ 0.1 A g⁻¹	this work

electrolyte interface, EIS measurements were performed. Fig. 12(a) shows Nyquist plots for CP900 and NF-MnO₂ (before and after GCD cycling stability). The obtained Nyquist plots contain a semi-circle at high frequencies, which is related to the electronic resistance within the electrode materials. The linear curve in the low-frequency region (Warburg, W) can be attributed to the diffusion controlled process in the electrolyte. The total impedance of the supercapacitor consists of electronic and ionic contributions. Where, the electronic contribution is related to the intrinsic electronic resistance of the particles and the interfacial resistances of particles-to-particles and particles-to-current collector. The ionic contribution is associated with the electrolyte resistances in the pores and the diffusion resistance of ions moving into small pores [32,39]. The vertical line at lower frequencies represents the facile ion diffusion in the structure which indicates an

ideal capacitance behavior for NF-MnO₂. In addition, the Bode plot (Fig. 12(b)) shows the correlation between the phase angle and the frequency response of a system. From which it is evident that the phase angle of NF-MnO₂ is at -73° which is very near to the phase angle of the ideal capacitor (-90°) [40].

The estimated equivalent series resistance (R_s), which is a combination of ionic resistance of the electrolyte, intrinsic resistance of active materials, and contact resistance at the active material-current collector interface, was obtained from the initial non-zero intersect with the real impedance axis at the beginning of the semicircle. NF-MnO₂ shows low R_s of 1.18 Ω , indicating the good conductivity of MnO₂ [21,22]. The charge transfer resistance (R_{ct}) can be estimated from the diameter semicircle in the high frequency range which is associated with the surface electrode properties. R_{ct} for NF-MnO₂ was found to be

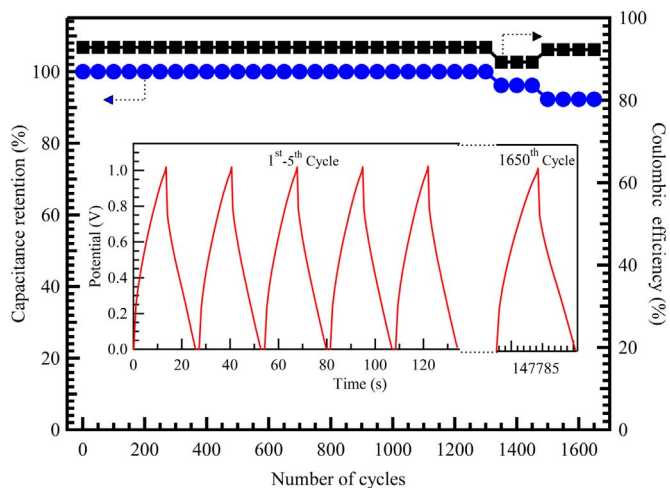


Fig. 11. Capacitance retention (left vs. bottom) and Coulombic efficiency (right vs. bottom) of NF-MnO₂ at 6 A g⁻¹ (Inset shows the charge–discharge of the 1st and 1650th cycles).

1.63 Ω, which is lower than that reported for MnO₂ (17 Ω) [10].

The relaxation time (τ) was calculated from the frequency (f^*) corresponding to the maximum of the imaginary component ($-Z''$) of the semi-circle in Nyquist plot using the following formula [41]:

Table 2

The calculated parameters obtained by fitting of the experimental impedance data before and after GCD stability for NF-MnO₂.

	R_s (Ω)	R_{ct} (Ω)	C (mF)	CPE (mF)	W (Ω)	S_E (cm ² g ⁻¹)	τ (s)
Before GCD stability	1.18	1.63	607.56	7.78	0.45	340	1.81
After GCD stability	1.27	1.97	587.49	6.12	0.59	408	1.81

$$\tau = \frac{1}{2 \pi f^*} \tag{6}$$

The τ values are found to be very low (1.81 s), indicating the good electrochemical capacitance properties and fast charge–discharge characteristic response. ESR and R_{ct} and other fitting parameters are summarized in Table 2.

The complex model of the capacitance was studied to show the dependence of the specific capacitance on frequency. The cell capacitance can be expressed as real and imaginary parts according to the following equations [42]:

$$C'(\omega) = \frac{-Z'(\omega)}{\omega |Z(\omega)|^2} \tag{7}$$

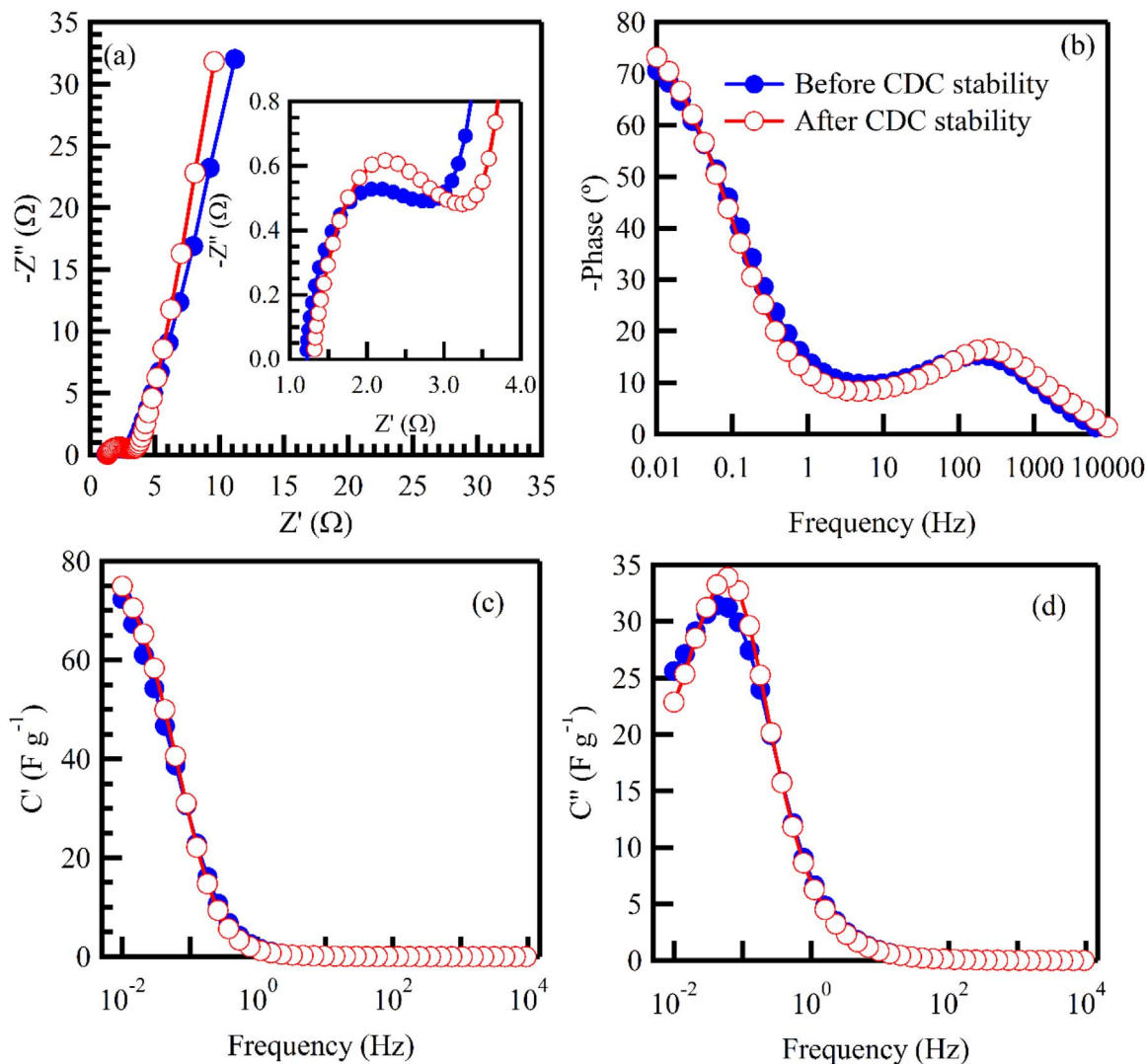


Fig. 12. Nyquist (a) and Bode (b) plots for NF-MnO₂; the inset is the curves at high frequency region, real (c) and imaginary (d) parts of capacitance as a function of frequency, before and after GCD cycling stability.

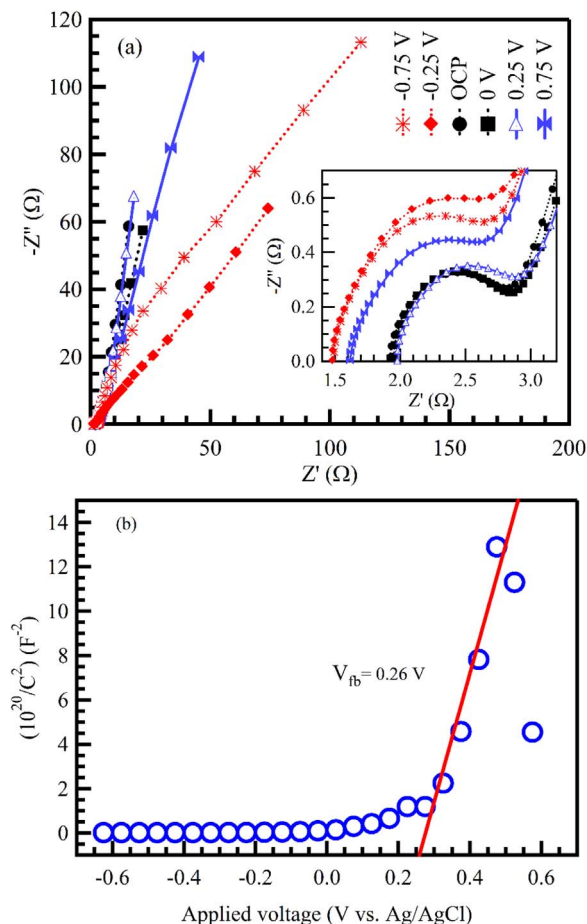


Fig. 13. Nyquist (a) and Mott-Schottky (b) plots for NF-MnO₂ under different applied potentials; the inset is the plot at high frequency region.

$$C''(\omega) = \frac{Z''(\omega)}{\omega|Z'(\omega)|^2} \quad (8)$$

where, C' and C'' represent the real and imaginary parts of the cell capacitance, respectively and $\omega = 2\pi f$. Plots of C' and C'' as functions of frequency for NF-MnO₂ are shown in Fig. 12(c, d).

The electrochemical active surface area can be calculated from Eq. (9) [40,43].

$$S_E = \frac{C_{dm}}{C_d} \quad (9)$$

where, C_d is a constant value of 20 $\mu\text{F cm}^{-2}$, C_{dm} is obtained from Nyquist impedance plot at low frequency (0.01 Hz) according to the equation $C_{dm} = 1/(2\pi f m Z'')$ [40,44], where f is the frequency. The calculated value of S_E is 340 $\text{m}^2 \text{g}^{-1}$. The electrochemical active surface area is found to be higher than the specific surface area obtained by N₂ adsorption technique (BET) as the former measurement includes the ions adsorption and the redox processes while the latter only measures on the N₂ adsorption-desorption. This is consistent with other reported works [45–47]. The excellent electrochemical properties of could be associated with its high electrochemical active surface area. EIS was repeated after GCD cycling stability to confirm the electrode stability as shown in Fig. 12. All calculated parameters after GCD stability are very close to their original values before cycling test, which indicates the highly stable behavior of NF-MnO₂ electrode (Table 2).

EIS was repeated under different operating voltages to obtain Mott-Schottky plots of NF-MnO₂ as shown in Fig. 13(a). The Mott-Schottky relation is given as [48]:

$$\frac{1}{C_{SCL}^2} = \frac{2}{e\epsilon\epsilon_0 N_D} \left(V - V_{fb} - \frac{kT}{e} \right) \quad (10)$$

where, C_{SCL} is the capacitance of the space charge layer, e is the charge of electron, ϵ_0 is free space permittivity ($8.85 \times 10^{-14} \text{ F cm}^{-1}$), ϵ is dielectric constant (32 for MnO₂ [49]), V is applied potential, V_{fb} is flat-band potential, N_D is donor density or donor concentration, k is Boltzmann constant and T is Kelvin temperature. Although, Mott-Schottky plot has a frequency-dependent slope, the extension of the linear part of the curve intersects the voltage axis at a point known as Schottky barrier or flat-band voltage. NF-MnO₂ shows positive slope (5×10^{17}) to indicate the n-type semiconductor characteristics. The flat band potential was obtained from the extrapolation of the linear fit of the Mott-Schottky plot (as shown in Fig. 13(b)) and found to be 0.26 V. V_{fb} of NF-MnO₂ is more positive than those obtained by other authors (0.16 V), indicating the better conductivity of NF-MnO₂ due to their small size [50] which is confirmed by XRD and UV-Vis data. In addition, it suggests that, the small size offers a higher number of crystalline planes exposed to the electrolyte. The N_D was determined from the slope of Mott-Schottky plot and found to be $7.6 \times 10^8 \text{ cm}^{-3}$.

4. Conclusions

MnO₂ nanoflower (NF-MnO₂) is successfully obtained by electrochemical cycling of heat treated zinc-carbon battery powder (CP900). The specific capacitance of NF-MnO₂ is 309 F g^{-1} at 0.1 A g^{-1} in a potential window of 0–1 V using 1 M Na₂SO₄ electrolyte, which is around six times higher than that of heat treated battery powder (54 F g^{-1}). Impedance spectrum of NF-MnO₂ shows very small resistance and high electrochemical active surface area (340 $\text{m}^2 \text{g}^{-1}$). NF-MnO₂ has high capacitance retentions of 93% over 1650 charge-discharge cycles, making it a promising electrode material for supercapacitors.

Acknowledgments

KF Chong and co-workers would like to acknowledge the funding from Ministry of Science, Technology and Innovation for the eScienceFund (06-01-16-SF0094) and Ministry of Education for the FRGS (RDU160118) fund.

References

- [1] G.A.M. Ali, O.A. Fouad, S.A. Makhlof, M.M. Yusoff, K.F. Chong, Co₃O₄/SiO₂ nanocomposites for supercapacitor application, *J. Solid State Electrochem.* 18 (2014) 2505–2512.
- [2] G.A.M. Ali, L.L. Tan, R. Jose, M.M. Yusoff, K.F. Chong, Electrochemical performance studies of MnO₂ nanoflowers recovered from spent battery, *Mater. Res. Bull.* 60 (2014) 5–9.
- [3] Y. Dai, K. Wang, J.Y. Xie, From spinel Mn₃O₄ to layered nanoarchitectures using electrochemical cycling and the distinctive pseudocapacitive behavior, *Appl. Phys. Lett.* 90 (2007).
- [4] S. Devaraj, N. Munichandraiah, Effect of crystallographic structure of MnO₂ on its electrochemical capacitance properties, *J. Phys. Chem. C* 112 (2008) 4406–4417.
- [5] D.P. Dubal, W.B. Kim, C.D. Lokhande, Surfactant assisted electrodeposition of MnO₂ thin films: improved supercapacitive properties, *J. Alloy. Compd.* 509 (2011) 10050–10054.
- [6] M.M. Yao, Z.H. Hu, Y.F. Liu, P.P. Liu, Z.H. Ai, O. Rudolf, 3D hierarchical mesoporous rose-like NiO nanosheets for high-performance supercapacitor electrodes, *J. Alloy. Compd.* 648 (2015) 414–418.
- [7] M.M. Momeni, Z. Nazari, A. Kazempour, M. Hakimiyan, S.M. Mirhoseini, Preparation of CuO nanostructures coating on copper as supercapacitor materials, *Surf. Eng.* 30 (2014) 775–778.
- [8] G.A.M. Ali, O.A. Fouad, S.A. Makhlof, M.M. Yusoff, K.F. Chong, Optical and electrochemical properties of Co₃O₄/SiO₂ nanocomposite, *Adv. Mater. Res.* 1133 (2016) 447–451.
- [9] G.A.M. Ali, O.A.G. Wahba, A.M. Hassan, O.A. Fouad, K.F. Chong, Calcium-based nanosized mixed metal oxides for supercapacitor application, *Ceram. Int.* 41 (2015) 8230–8234.
- [10] D.P. Dubal, C.D. Lokhande, Significant improvement in the electrochemical performances of nano-nest like amorphous MnO₂ electrodes due to Fe doping, *Ceram. Int.* 39 (2013) 415–423.
- [11] R.B. Rakhi, D.K. Cha, W. Chen, H.N. Alshareef, Electrochemical energy storage

- devices using electrodes incorporating carbon nanocoils and metal oxides nanoparticles, *J. Phys. Chem. C* 115 (2011) 14392–14399.
- [12] N. Li, X. Zhu, C. Zhang, L. Lai, R. Jiang, J. Zhu, Controllable synthesis of different microstructured MnO₂ by a facile hydrothermal method for supercapacitors, *J. Alloy. Compd.* 692 (2017) 26–33.
- [13] C.C.B.M. de Souza, J.A.S. Tenorio, Simultaneous recovery of zinc and manganese dioxide from household alkaline batteries through hydrometallurgical processing, *J. Power Sources* 136 (2004) 191–196.
- [14] G.A.M. Ali, M.M. Yusoff, Y.H. Ng, H.N. Lim, K.F. Chong, Potentiostatic and galvanostatic electrodeposition of manganese oxide for supercapacitor application: a comparison study, *Curr. Appl. Phys.* 15 (2015) 1143–1147.
- [15] V. Subramanian, H.W. Zhu, B.Q. Wei, Nanostructured MnO₂: hydrothermal synthesis and electrochemical properties as a supercapacitor electrode material, *J. Power Sources* 159 (2006) 361–364.
- [16] Y.J. Yang, C.D. Huang, Effect of synthetic conditions, morphology, and crystallographic structure of MnO₂ on its electrochemical behavior, *J. Solid State Electrochem.* 14 (2010) 1293–1301.
- [17] S.C. Pang, S.F. Chin, C.Y. Ling, Controlled synthesis of manganese dioxide nanostructures via a facile hydrothermal route, *J. Nanomater.* 2012 (2012) 1–7.
- [18] X. Wang, X. Wang, W. Huang, P.J. Sebastian, S. Gamboa, Sol-gel template synthesis of highly ordered MnO₂ nanowire arrays, *J. Power Sources* 140 (2005) 211–215.
- [19] D.P. Dubal, D.S. Dhawale, T.P. Gujar, C.D. Lokhande, Effect of different modes of electrodeposition on supercapacitive properties of MnO₂ thin films, *Appl. Surf. Sci.* 257 (2011) 3378–3382.
- [20] G.A.M. Ali, M.M. Yusoff, K.F. Chong, Electrochemical Properties of Electrodeposited MnO₂ Nanoparticles, *Adv. Mater. Res.* 1113 (2015) 550–553.
- [21] D.P. Dubal, D.S. Dhawale, R.R. Salunkhe, C.D. Lokhande, Conversion of interlocked cube-like Mn₃O₄ into nanoflakes of layered birnessite MnO₂ during supercapacitive studies, *J. Alloy. Compd.* 496 (2010) 370–375.
- [22] D.P. Dubal, D.S. Dhawale, R.R. Salunkhe, C.D. Lokhande, Conversion of chemically prepared interlocked cubelike Mn₃O₄ to birnessite MnO₂ using electrochemical cycling, *J. Electrochem. Soc.* 157 (2010) A812–A817.
- [23] G. Belardi, R. Lavecchia, F. Medici, L. Piga, Thermal treatment for recovery of manganese and zinc from zinc-carbon and alkaline spent batteries, *Waste Manag.* 32 (2012) 1945–1951.
- [24] J. Nan, D. Han, M. Cui, M. Yang, L. Pan, Recycling spent zinc manganese dioxide batteries through synthesizing Zn-Mn ferrite magnetic materials, *J. Hazard. Mater.* 133 (2006) 257–261.
- [25] S.-M. Shin, J.-G. Kang, D.-H. Yang, J.-S. Sohn, Development of metal recovery process from alkaline manganese batteries in sulfuric acid solutions, *Mater. Trans., JIM* 48 (2007) 244–248.
- [26] G. Belardi, P. Ballirano, M. Ferrini, R. Lavecchia, F. Medici, L. Piga, A. Scoppettuolo, Characterization of spent zinc-carbon and alkaline batteries by SEM-EDS, TGA/DTA and XRPD analysis, *Thermochim. Acta* 526 (2011) 169–177.
- [27] B. Djurfors, J. Broughton, M. Brett, D. Ivey, Electrochemical oxidation of Mn/MnO films: mechanism of porous film growth, *J. Electrochem. Soc.* 153 (2006) A64–A68.
- [28] B. Djurfors, J. Broughton, M. Brett, D. Ivey, Microstructural characterization of porous manganese thin films for electrochemical supercapacitor applications, *J. Mater. Sci.* 38 (2003) 4817–4830.
- [29] A.L. Patterson, The Scherrer formula for X-ray particle size determination, *Phys. Rev.* 56 (1939) 978–982.
- [30] H. Lin, C.P. Huang, W. Li, C. Ni, S.I. Shah, Y.H. Tseng, Size dependency of nanocrystalline TiO₂ on its optical property and photocatalytic reactivity exemplified by 2-chlorophenol, *Appl. Catal. B* 68 (2006) 1–11.
- [31] G.A.M. Ali, O.A. Fouad, S.A. Makhlof, Structural, optical and electrical properties of sol-gel prepared mesoporous Co₃O₄/SiO₂ nanocomposites, *J. Alloy. Compd.* 579 (2013) 606–611.
- [32] D.D. Zhao, Z. Yang, L.Y. Zhang, X.L. Feng, Y.F. Zhang, Electrodeposited manganese oxide on nickel foam-supported carbon nanotubes for electrode of supercapacitors, *Electrochem. Solid-State Lett.* 14 (2011) A93–A96.
- [33] P. Yu, X. Zhang, D. Wang, L. Wang, Y. Ma, Shape-controlled synthesis of 3D hierarchical MnO₂ nanostructures for electrochemical supercapacitors, *Cryst. Growth Des.* 9 (2008) 528–533.
- [34] T. Cottineau, M. Toupin, T. Delahaye, T. Brousse, D. Belanger, Nanostructured transition metal oxides for aqueous hybrid electrochemical supercapacitors, *Appl. Phys. A* 82 (2006) 599–606.
- [35] S. Devaraj, N. Munichandraiah, Electrochemical supercapacitor studies of nanostructured α-MnO₂ synthesized by microemulsion method and the effect of annealing, *J. Electrochem. Soc.* 154 (2007) A80–A88.
- [36] D.P. Dubal, D.S. Dhawale, R.R. Salunkhe, C.D. Lokhande, A novel chemical synthesis of Mn₃O₄ thin film and its stepwise conversion into birnessite MnO₂ during super capacitive studies, *J. Electroanal. Chem.* 647 (2010) 60–65.
- [37] J. Jiang, A. Kucernak, Electrochemical supercapacitor material based on manganese oxide: preparation and characterization, *Electrochim. Acta* 47 (2002) 2381–2386.
- [38] Y. Zhang, G.-Y. Li, Y. Lv, L.-Z. Wang, A.-Q. Zhang, Y.-H. Song, B.-L. Huang, Electrochemical investigation of MnO₂ electrode material for supercapacitors, *Int. J. Hydrogen Energy* 36 (2011) 11760–11766.
- [39] A.G. Pandolfo, A.F. Hollenkamp, Carbon properties and their role in supercapacitors, *J. Power Sources* 157 (2006) 11–27.
- [40] G.A.M. Ali, S.A. Makhlof, M.M. Yusoff, K.F. Chong, Structural and electrochemical characteristics of graphene nanosheets as supercapacitor electrodes, *Rev. Adv. Mater. Sci.* 40 (2015) 35–43.
- [41] G.S. Gund, D.P. Dubal, B.H. Patil, S.S. Shinde, C.D. Lokhande, Enhanced activity of chemically synthesized hybrid graphene oxide/Mn₃O₄ composite for high performance supercapacitors, *Electrochim. Acta* 92 (2013) 205–215.
- [42] R.A. Aziz, I.I. Misnon, K.F. Chong, M.M. Yusoff, R. Jose, Layered sodium titanate nanostructures as a new electrode for high energy density supercapacitors, *Electrochim. Acta* 113 (2013) 141–148.
- [43] S. Chou, F. Cheng, J. Chen, Electrodeposition synthesis and electrochemical properties of nanostructured γ-MnO₂ films, *J. Power Sources* 162 (2006) 727–734.
- [44] G.A.M. Ali, M.M. Yusoff, K.F. Chong, Graphene: electrochemical production and its energy storage properties, *ARPN J. Eng. Appl. Sci.* 11 (2016) 9712–9717.
- [45] M. Lukaszewski, M. Soszko, A. Czerwiński, Electrochemical methods of real surface area determination of noble metal electrodes—an overview, *Int. J. Electrochem. Sci.* 11 (2016) 4442–4469.
- [46] S. Trasatti, O. Petrii, Real surface area measurements in electrochemistry, *J. Electroanal. Chem.* 327 (1992) 353–376.
- [47] B. Beden, C. Lamy, N. De Tacconi, A. Arvia, The electrooxidation of CO: a test reaction in electrocatalysis, *Electrochim. Acta* 35 (1990) 691–704.
- [48] W.J. Basirun, M. Sookhikian, S. Baradaran, Z. Endut, M.R. Mahmoudian, M. Ebadi, R. Yousefi, H. Ghadimi, S. Ahmed, Graphene oxide electrocatalyst on MnO₂ air cathode as an efficient electron pump for enhanced oxygen reduction in alkaline solution, *Sci. Rep.* 5 (2015) 1–7.
- [49] J.W. Murray, The interaction of metal ions at the manganese dioxide-solution interface, *Geochim. Cosmochim. Acta* 39 (1975) 505–519.
- [50] L.M. Gassa, H.T. Mishima, B.A.L. de Mishima, J.R. Vilche, An electrochemical impedance spectroscopy study of electrodeposited manganese oxide films in borate buffers, *Electrochim. Acta* 42 (1997) 1717–1723.